

Article

Recrystallization and Production of Spherical Submicron Particles of Sulfasalazine Using a Supercritical Antisolvent Process

Wei-Yi Wu and Chie-Shaan Su *

Department of Chemical Engineering and Biotechnology, National Taipei University of Technology, 1, Sec. 3, Zhongxiao E. Rd., Taipei 10608, Taiwan; torpedodesign@yahoo.com.tw

* Correspondence: cssu@ntut.edu.tw; Tel.: +886-227712171 (ext. 2532)

Received: 13 June 2018; Accepted: 13 July 2018; Published: 18 July 2018



Abstract: In this study, the recrystallization and production of spherical submicron particles of sulfasalazine, an active pharmaceutical ingredient (API), were performed using the supercritical antisolvent (SAS) process, a nonconventional crystallization technique. Sulfasalazine was dissolved in tetrahydrofuran (THF), and supercritical carbon dioxide (CO₂) served as the antisolvent. The effects of operating parameters on the SAS process, including the operating pressure, solution concentration, solution flowrate, CO₂ flowrate, and spraying nozzle diameter, at two operating temperatures were examined. The solid-state characteristics of sulfasalazine before and after the SAS process, including particle size, crystal habit, and crystal form, were analyzed using a scanning electron microscope (SEM), powder X-ray diffractometer (PXRD), and differential scanning calorimeter (DSC). A higher operating temperature, intermediate operating pressure, higher CO₂ flowrate, and lower solution flowrate are recommended to obtain spherical particles of sulfasalazine. The effects of the solution concentration and spraying nozzle diameter on the SAS process were negligible. Under optimal conditions, spherical sulfasalazine crystals with a mean size of 0.91 μm were generated, and this study demonstrated the feasibility for tuning the solid-state characteristics of API through the SAS process.

Keywords: sulfasalazine; supercritical antisolvent; recrystallization; spherical; submicron

1. Introduction

In the pharmaceutical industry, the modification of the solid-state characteristics of active pharmaceutical ingredients (APIs) is crucial to overcome poor aqueous solubility and provide suitable powder characteristics in downstream processing [1]. Reducing the particle size, modifying the crystal habit, and designing the crystal form of APIs are common approaches to improve the bioavailability of APIs with poor water solubility and to enhance powder handling in the formulation design [2]. For example, Jog and Burgess reviewed the application of pharmaceutical amorphous nanoparticles in designing novel drug delivery systems and summarized the particle manufacturing techniques [3]. Modi et al. investigated the effect of crystal habit on intrinsic dissolution behavior and demonstrated the effect of particle-level properties and the surface molecular environment on the intrinsic dissolution rate [4]. Chattoraj and Sun summarized different crystal and particle engineering strategies for improving powder flow and compression properties for continuous tablet manufacturing through direct compression [5]. Pudasaini et al. investigated the effect of solvent selection on crystal habit to overcome problems in needle-like crystal production through a conventional crystallization process [6]. In general, the production of smaller particles with a spherical crystal habit, which provides an enhanced dissolution profile and superior powder flowability, is favorable for drug design and development. In addition, the application of supercritical fluid crystallization, a nonconventional

crystallization technique, for the micronization and particle design of APIs has also been discussed and reviewed in the literature [7–9].

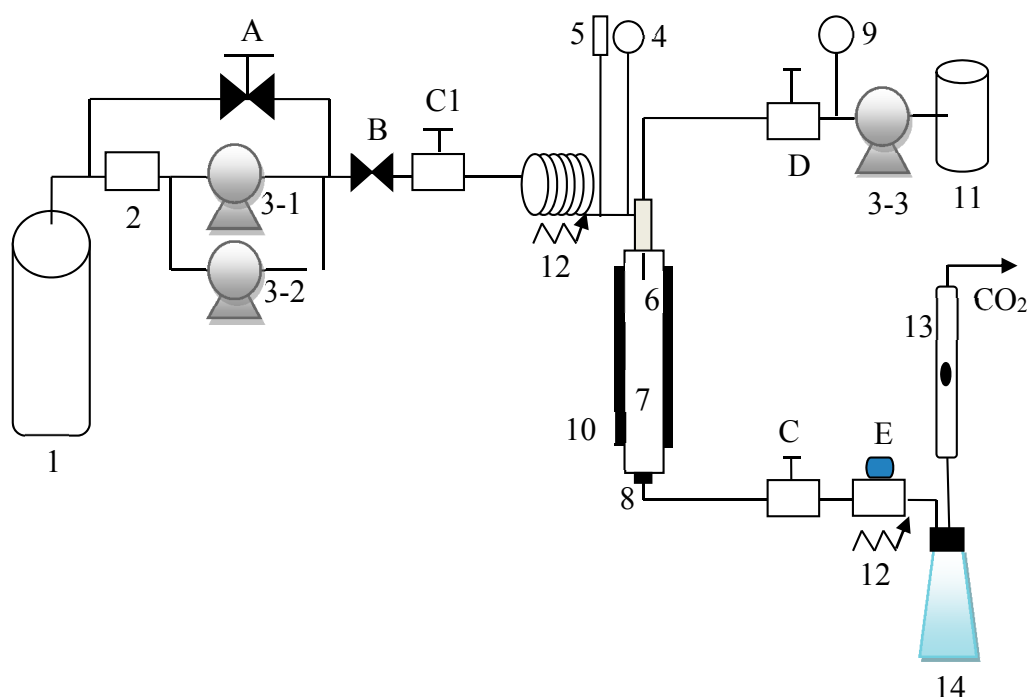
In supercritical fluid crystallization techniques, depending on the mechanism and role of supercritical fluids, different processes have been developed, such as the rapid expansion of supercritical solution (RESS), supercritical antisolvent (SAS), supercritical assisted atomization (SAA), and particle from gas saturated solution (PGSS) [10]. The supercritical fluid is employed as the solvent, antisolvent, dissolved solute, and spraying-assisted cosolvent in RESS, SAS, PGSS, and SAA, respectively. In pharmaceutical applications, SAS is frequently used owing to the low solubility of pharmaceutical solids in supercritical fluids [11]. Because of the advantages of carbon dioxide (CO₂), namely its nontoxicity, nonflammability, environmental friendliness, and mild supercritical conditions, CO₂ is recognized as a green solvent and is commonly used in the SAS process. In the literature, the SAS process has been demonstrated to be superior to the conventional crystallization process for the modification of the solid-state properties of pharmaceutical and biological compounds, such as baicalein, curcumin, palmitoylethanolamide, quercetin, β -carotene, ellagic acid, etoposide, indomethacin, mangiferin, rutin, tetracycline, aescin, carbamazepine, curcumin, gefitinib, levofloxacin, primidone, warfarin, and naringenin [12–31]. Using SAS, crystals with sizes in the range of microns to nanometers, regular crystal habit, and narrow size distribution can be produced. These improved powder characteristics benefit drug design and the downstream formulation process by enhancing the dissolution behavior and powder handling procedure.

In this study, sulfasalazine was selected as a model API, and the recrystallization of sulfasalazine through the SAS process was conducted to investigate whether this process can be used to control solid-state characteristics. Sulfasalazine is a sulfonamide used to treat rheumatoid arthritis, ulcerative colitis, and Crohn's disease. In our preliminary study, we performed a solvent selection and reported the temperature effect in the SAS recrystallization of sulfasalazine [32]. To further investigate the mechanism of the SAS recrystallization of sulfasalazine, the effect of the operating pressure, solution concentration, solution flowrate, CO₂ flowrate, and nozzle diameter at two selected operating temperatures were systematically compared and discussed. The crystal habit, particle size, and crystal form of recrystallized sulfasalazine were examined and compared. Subsequently, the appropriate operation conditions for obtaining spherical submicron particles of sulfasalazine were finally summarized.

2. Materials and Methods

CO₂, which was used as the supercritical antisolvent, was supplied by Cheng-Feng Gas Co. (Taipei, Taiwan), with a minimum purity of 99.5%. The API sulfasalazine (CAS number: 599-79-1) was supplied by Sigma-Aldrich Co. (St. Louis, MO, USA), with a minimum purity of 98%. Tetrahydrofuran (THF), which was used as the solvent, was purchased from JT Baker (Center Valley, PA, USA), with a minimum purity of 99.5%. All chemicals were used without further purification. The experimental apparatus for SAS is described in detail in our previous study [30–32]. As shown in Figure 1, the experimental apparatus depicted consisted of two high-performance liquid chromatography (HPLC) pumps (components 3-1 and 3-2) for delivering the supercritical CO₂, and an HPLC pump (component 3-3) for delivering the sulfasalazine solution. The pressure and temperature of the experimental system were controlled using a back pressure regulator (valve A) and an electrical heating jacket (component 10), respectively. The pressure and temperature of the system were measured using a pressure transducer (component 4) and a thermocouple (component 5), with the resolutions of 0.1 K and 0.1 bar, respectively. The CO₂ flowrate was controlled using a micrometering valve (valve E) and was measured using a rotameter under ambient conditions (component 13). Sulfasalazine crystallization occurred in a precipitator (component 7). The volume of the precipitator was 70 mL, and a stainless steel frit was installed at the bottom of the precipitator for sample collection. The SAS process was initiated with the injection of supercritical CO₂ and the pure solvent (THF) into the precipitator until a steady state was achieved. Subsequently, the liquid feed flow was switched to the sulfasalazine solution for API crystallization. After API crystallization, supercritical drying was

performed by delivering supercritical CO₂ continuously to eliminate the residual solvent inside the precipitator. Subsequently, the precipitator was depressurized, and the samples on the stainless steel frit were collected for further analysis.



Valve Description	Component Description	
A: Back pressure regulator	1: CO ₂ cylinder	8: Filter
B: Check valve	2: Cooler	9: Pressure gauge
C: Needle valve	3: HPLC pump	10: Heating jacket
D: Ball valve	4: Pressure transducer	11: Solution reservoir
E: Micrometering valve	5: Thermometer	12: Heating tape
-	6: Nozzle	13: Rotameter
-	7: Precipitator	14: Solvent trap

Figure 1. Experimental apparatus of the supercritical antisolvent (SAS) process.

To investigate the particle size, crystal habit, thermal properties, and crystal form of sulfasalazine, the original and recrystallized sulfasalazine were analyzed using a scanning electron microscope (SEM), powder X-ray diffractometer (PXRD), and differential scanning calorimeter (DSC). For SEM analysis, crystals were fixed on conductive adhesive tape and were sputtered with a thin film of gold. For comparison of crystal habits, images of sulfasalazine crystals were captured through an SEM (HITACHI, S-3000H). In addition, SEM images after sharpening were used to calculate the mean particle size of sulfasalazine crystals through the analysis of at least 200 crystals using ImageJ software. For the needle-like crystal, the needle length was recorded and reported. To determine the crystal structure, PXRD data were collected from 5° to 50° at a scanning rate of 3°/min by using a PXRD (PANalytical X'pert). To determine the thermal properties of the crystals, a DSC (PerkinElmer, Jade DSC) was used, and the samples were heated from 50 °C to 270 °C at a heating rate of 10 °C/min.

3. Results and Discussion

The preliminary results for the recrystallization of sulfasalazine through SAS are described in our previous study [32]. In SAS, the THF was selected as an appropriate solvent when supercritical CO₂ served as the antisolvent, and the operating temperature exerted a significant effect on the crystal habit

of recrystallized sulfasalazine [32]. To further investigate the mechanism of the SAS recrystallization of sulfasalazine, 16 SAS experiments were designed, as depicted in Table 1. The effects of the operating pressure, solution concentration, CO₂ flowrate, solution flowrate, and spraying nozzle diameter at two designed operating temperatures were analyzed and discussed. The results of the SAS recrystallization, including the yield, crystal form, mean size, and crystal habit, are also listed in Table 1. In Table 1, Exp. 1 and Exp. 9 are the experimental results obtained in our previous study [32].

Table 1. Results of the SAS study of sulfasalazine using THF as the solvent.

Exp. No.	Operating Condition						Result			
	T (°C)	P (bar)	Conc. (%)	F _{CO₂} (L/min)	F _{soln} (mL/min)	N (μm)	Yield (%)	Crystal Form	Mean size (μm)	Crystal Habit
Ori	—	—	—	—	—	—	—	I	6.10	Irregular
1 ^(a)	35	100	90	4	0.5	100	91.8	II	88.9	Needle-like/Nanocluster
2	35	80	90	4	0.5	100	97.4	II	53.6	Needle-like/Nanocluster
3	35	120	90	4	0.5	100	92.9	II	71.4	Needle-like
4	35	100	30	4	0.5	100	87.4	II	60.3	Needle-like/Nanocluster
5	35	100	60	4	0.5	100	90.1	II	40.4	Needle-like/Nanocluster
6	35	100	90	2	0.5	100	91.2	II	79.2	Needle-like/Nanocluster
7	35	100	90	4	1.0	100	93.7	II	36.6	Needle-like
8	35	100	90	4	0.5	200	94.6	II	53.8	Needle-like/Nanocluster
9 ^(a)	55	100	90	4	0.5	100	91.0	I + II	1.03	Spherical
10	55	80	90	4	0.5	100	89.1	II	4.32	Rod-like
11	55	120	90	4	0.5	100	91.4	I + II	2.23	Spherical/irregular
12	55	100	30	4	0.5	100	80.0	I + II	1.00	Spherical
13	55	100	60	4	0.5	100	83.7	I + II	0.91	Spherical
14	55	100	90	2	0.5	100	94.4	I + II	2.80	Spherical/irregular
15	55	100	90	4	1.0	100	93.3	I + II	1.37	Spherical/irregular
16	55	100	90	4	2.0	100	92.7	II	32.1	Needle-like
17	55	100	90	4	0.5	50	86.0	I + II	0.95	Spherical
18	55	100	90	4	0.5	200	81.9	I + II	1.17	Spherical

^(a) Results from our previous study [32].

In this study, the effects of operating parameters on the SAS recrystallization of sulfasalazine were systematically investigated. The modification of the solid-state characteristics of sulfasalazine was discussed, and the feasible operating region for producing spherical crystals was summarized. To discuss the SAS recrystallization at 35 °C, the SAS results obtained at different operating pressures (80, 100, and 120 bar), solution concentrations (30%, 60%, and 90% saturation), CO₂ flowrates (2 and 4 L/min), solution flowrates (0.5 and 1 mL/min), and spraying nozzle diameters (100 and 200 μm) are listed in Table 1 (Exp. 2–8). These SAS experiments produced needle-like crystals with nanoclusters, except for Exp. 3 and Exp. 7, in which only needle-like crystals were produced. The crystal habits of needle-like sulfasalazine analyzed using the SEM are presented in Figure 2a,b for Exp. 5 and 7, respectively. The average needle length of the needle-like crystals obtained from these SAS experiments was between 40 and 90 μm. The SEM image of the sulfasalazine nanoclusters from Exp. 5 are depicted in Figure 2c. In this experiment, the primary particles in the nanoclusters were approximately 200 nm. To further characterize the crystal properties of the nanocluster, a comparison of sulfasalazine crystals analyzed using a DSC thermogram in Exp. 7 and 8 is provided in the supplementary material as Figure S1. For Exp. 8, an additional exothermic peak of approximately 130 °C indicated a recrystallization process in which nanoclusters were amorphous. These amorphous nanoclusters might have been generated in the early stage of the SAS recrystallization process due to extremely high supersaturation. Furthermore, according to Table 1, spherical sulfasalazine crystals were obtained at 55 °C. According to the PXRD comparison of the original and SAS-processed sulfasalazine in Figure S2 in the supplementary material, the production of spherical crystals can be attributed to the modification of the polymorphic form of sulfasalazine in the SAS process. As presented in Figure S2, compared with the original form I crystals, needle-like sulfasalazine exhibited form II characteristics according to the PXRD results, and spherical sulfasalazine was determined to be a mixture of form I and II. SAS is a high supersaturation crystallization process. When SAS was operated at 35 °C, only form II nuclei were generated and they grew unidirectionally, resulting in the production of needle-like crystals. However, when operated at 55 °C, both form I and form II nuclei were generated. The crystal growth of both forms interfered with their unidirectional growth, thus producing spherical particles.

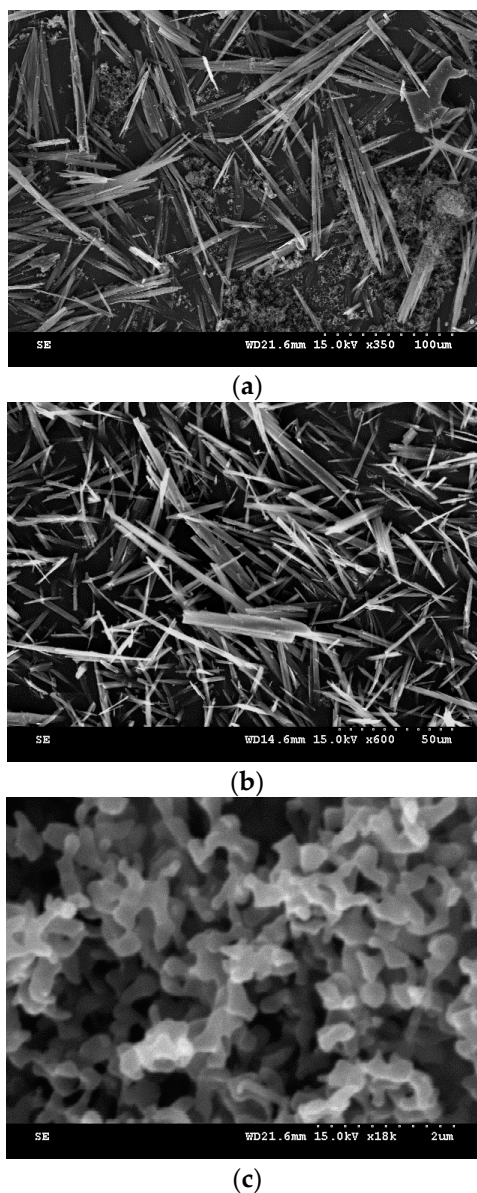


Figure 2. SEM images of sulfasalazine crystals: (a) Needle-like particles obtained from Exp. 5; (b) needle-like particles obtained from Exp. 7; and (c) nanoclusters obtained from Exp. 5.

To further analyze the optimum operation condition for obtaining spherical sulfasalazine at 55 °C, SAS experiments at different operating pressures (80, 100, and 120 bar), solution concentrations (30%, 60%, and 90% saturated), CO₂ flowrates (2 and 4 L/min), solution flowrates (0.5, 1, and 2 mL/min), and spraying nozzle diameters (50, 100, and 200 μm) were designed, as depicted in Table 1 (Exp. 10–18). The crystallization yield, mean size, crystal habit, and crystal form of sulfasalazine crystals obtained from the SAS experiments at 55 °C are also listed in Table 1. The effects of operating parameters on the mean particle size of sulfasalazine are illustrated in Figure 3. According to Table 1 and Figure 3, the operating pressure, CO₂ flowrate, and solution flowrate significantly affected the mean size and crystal habit of sulfasalazine crystals, whereas the solution concentration and spray nozzle diameter exerted negligible effects. Figure 3a reveals the effect of the operating pressure on the mean size of sulfasalazine. Three SAS experiments were performed at 80 (Exp. 10), 100 (Exp. 9), and 120 bar (Exp. 11). A decrease in the mean size from 4.32 to 1.03 μm was observed, with a corresponding increase in the pressure from 8 to 10 MPa. However, with a further increase in the operating pressure to 12 MPa, the particle size increased to 2.23 μm. In addition, the crystal habits were also altered

from rod-like and spherical to spherical and irregularly shaped when the SAS process was operated at 80, 100, and 120 bar, as depicted in Figure 4a–c. The trend of pressure effects in this SAS study was consistent with that obtained in a study that conducted the SAS processing of naringenin [29]. The effect of the operating pressure can be determined by applying principles of phase equilibria [33]. Figure 5 presents the predicted vapor-liquid equilibrium (VLE) of CO₂ + THF at 55 °C using the Predictive Soave-Redlich-Kwong (PSRK) equation of state. The feasibility of the PSRK equation of state for predicting the VLE of CO₂ + THF has been verified in our previous study [32]. The operating pressures of 80, 100, and 120 bar were also plotted on this diagram. When the operating pressure increased from 80 bar to 100 bar, the operating regions shifted from the two-phase region to above the mixture critical point (MCP), which is a favorable condition for the production of smaller crystals in the SAS recrystallization process. When the operating pressure was further increased from 100 to 120 bar, both pressures were above the MCP, meaning that the crystallization mechanisms of these two pressure experiments were similar. However, when the operating pressure is considerably above the MCP, the saturated solubility of sulfasalazine in a supercritical solution increases. This saturated solubility increasingly inhibits supersaturation during crystallization; thus, it is not conducive for producing small sulfasalazine crystals.

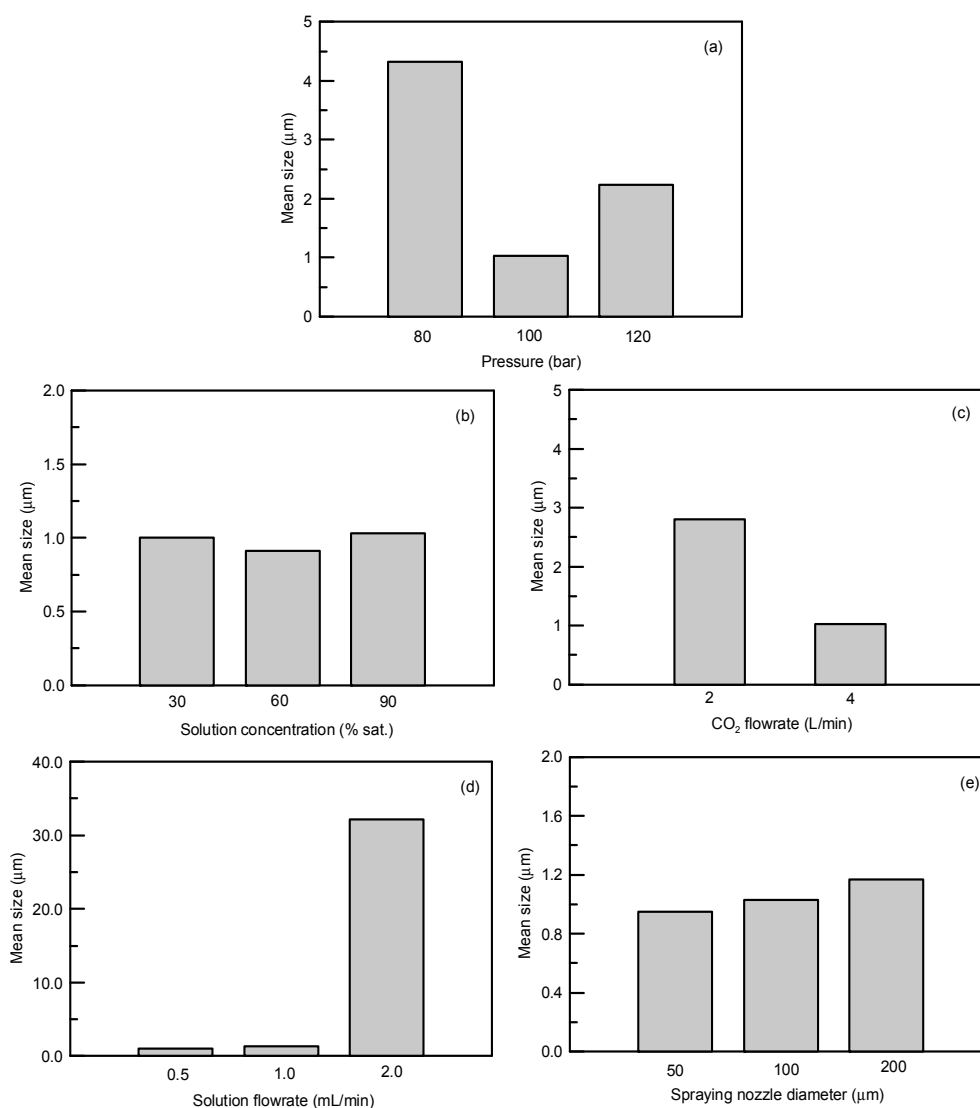


Figure 3. Effects of the (a) operating pressure, (b) solution concentration, (c) CO₂ flowrate, (d) solution flowrate, and (e) spraying nozzle diameter on the mean particle size of SAS-processed sulfasalazine.

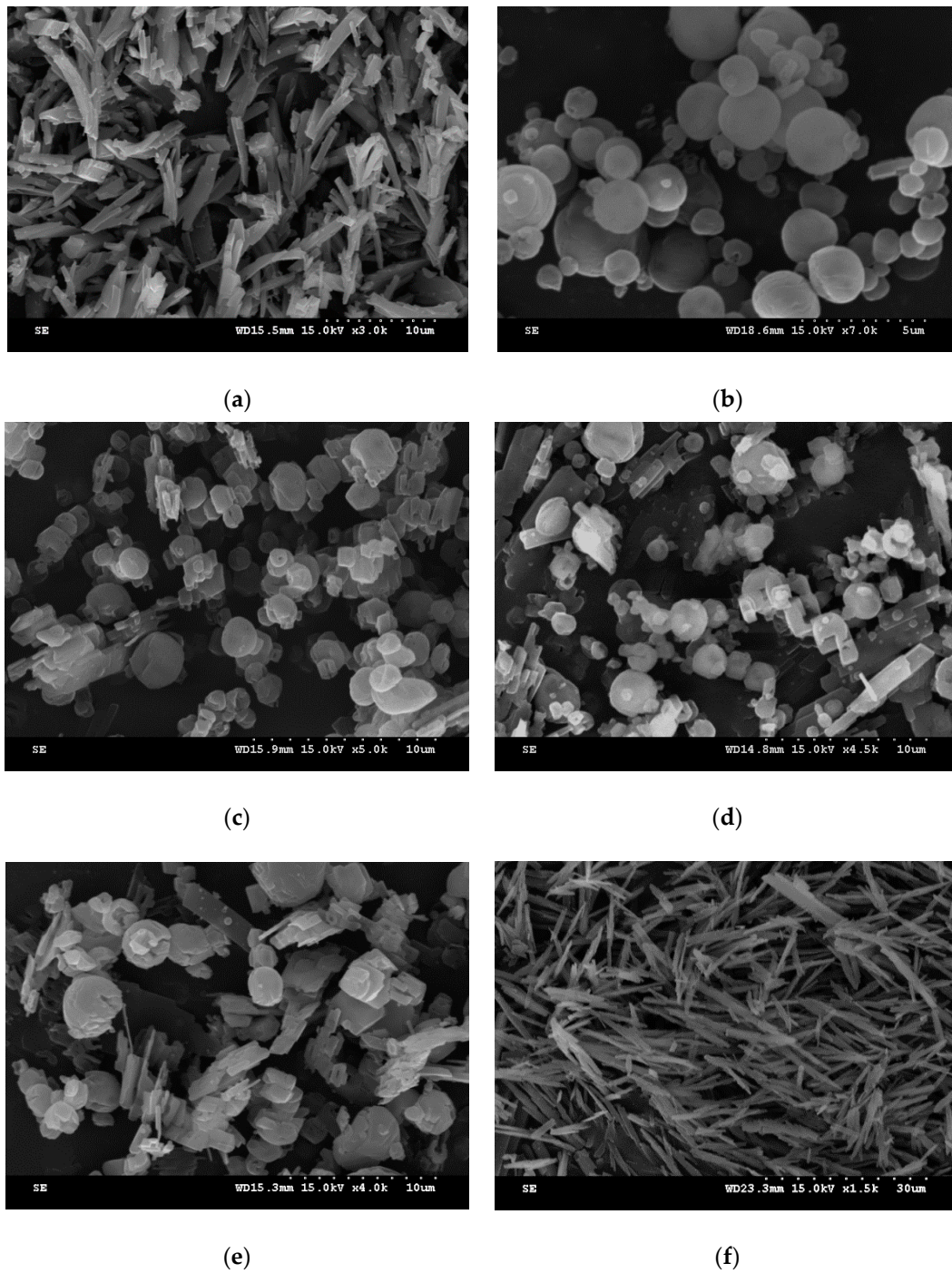


Figure 4. SEM images of sulfasalazine crystals: (a) Rod-like particles obtained from Exp. 10; (b) spherical particles obtained from Exp. 9; (c) spherical and irregular particles obtained from Exp. 11; (d) spherical and irregular particles obtained from Exp. 14; (e) spherical and irregular particles obtained from Exp. 15; and (f) needle-like particles obtained from Exp. 16.

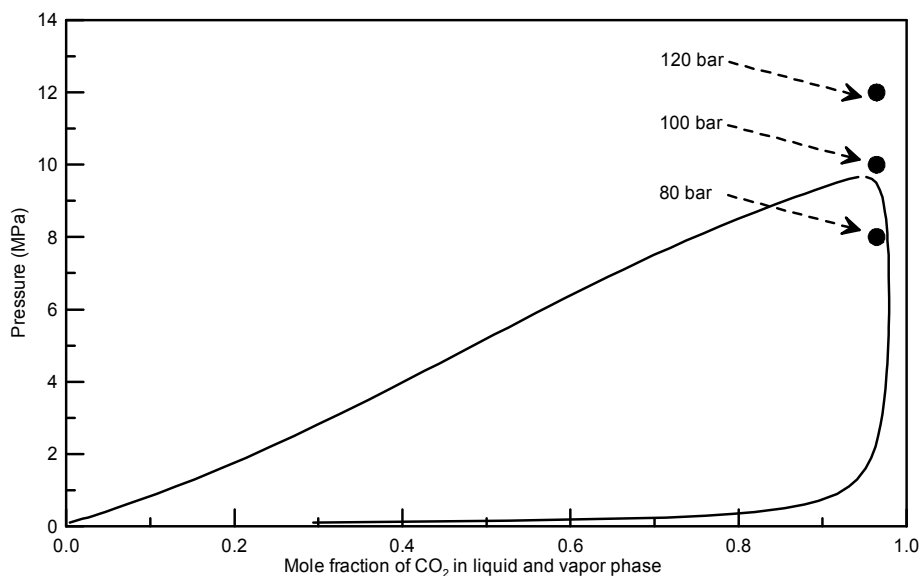


Figure 5. Predicted vapor-liquid equilibrium (VLE) locus for the binary mixture of CO₂ and THF using the Predictive Soave-Redlich-Kwong (PSRK) equation of state at 55 °C (● operation point at three experimental pressures).

Figure 3c,d present the effect of the CO₂ flowrates of 2 and 4 L/min and solution flowrates of 0.5, 1, and 2 mL/min on the mean size of sulfasalazine. A lower solution flowrate and higher CO₂ flowrate led to the production of smaller sulfasalazine crystals. A lower solution flowrate and higher CO₂ flowrate indicated a higher antisolvent to solvent ratio in the precipitator, resulting in a faster supersaturation of the solute, and a lower saturated solubility of sulfasalazine in this fluid, which caused the rapid nucleation and formation of small crystals. Similar results have also been reported in the literature [16,27,29]. In addition, the CO₂ flowrate and solution flowrate had considerable influence on the crystal habit of recrystallized sulfasalazine. In Figure 4b,d, the crystal habit of recrystallized sulfasalazine crystals obtained from the SAS experiments were compared at different CO₂ flowrates. Figure 4b,e,f present a comparison of the crystal habit of sulfasalazine crystals in Exp. 9, 15, and 16 at solution flowrates of 0.5, 1, and 2 mL/min, respectively. In Exp. 9, which had the lowest solution flowrate and the highest CO₂ flowrate, spherical sulfasalazine was successfully produced. However, with an increased solution flowrate or decreased CO₂ flowrate, which reduced the antisolvent-to-solvent ratio in the precipitator, irregular crystals began to form. When the solution flowrate was increased to 2 mL/min (Exp. 16), only needle-like particles were produced. In this SAS study, under optimal conditions, spherical sulfasalazine crystals with a mean size of 0.91 μm were produced. The comparisons of crystal habit and particle size distribution presented in Figure 6 indicate that the SAS process was efficient in manipulating the solid-state characteristics of sulfasalazine. Furthermore, the observed crystallization recoveries were all higher than 80%, indicating that the selected solvent (THF) and antisolvent (supercritical CO₂) system were appropriate from an engineering perspective. Finally, to verify the reproducibility of our SAS results, two experiments using the experimental condition of Exp. 9 were conducted. The measured mean size of these two repeated SAS experiments were 0.99 and 0.92 μm, which is quite close to our reported size for Exp. 9 (1.03 μm).

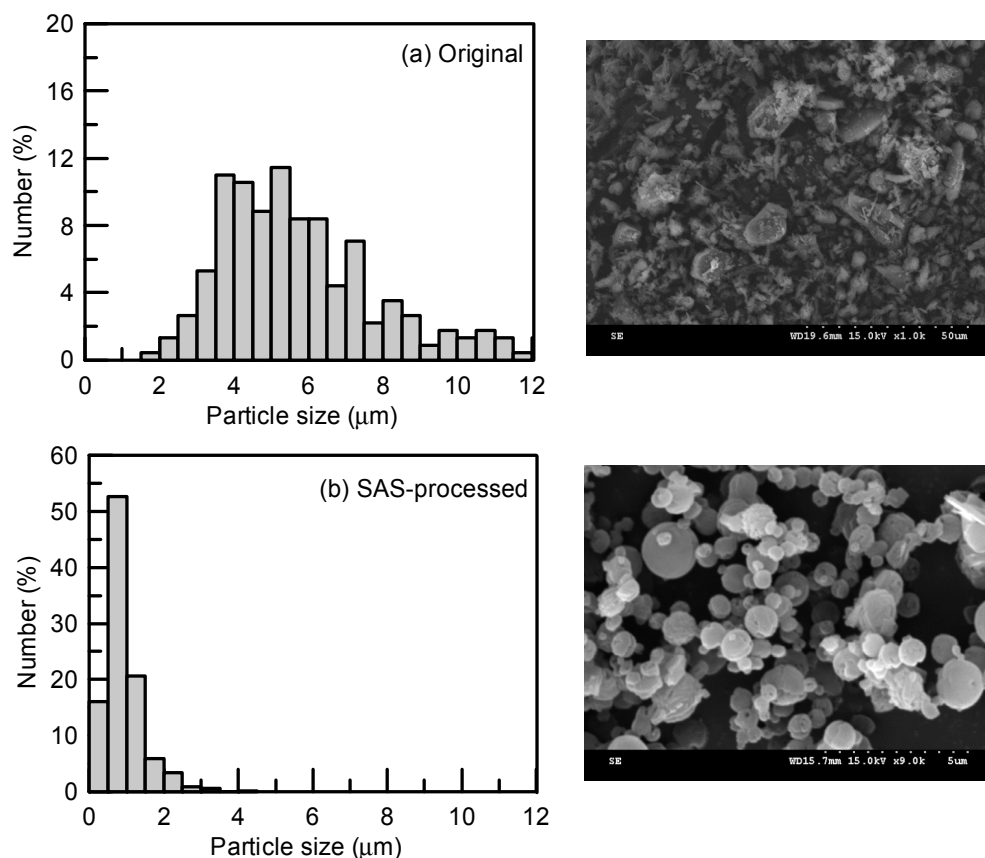


Figure 6. Particle size distribution and crystal habit of sulfasalazine crystals before and after the SAS process: (a) Original and (b) spherical particles obtained from Exp. 13.

4. Conclusions

Spherical submicron particles of sulfasalazine were successfully generated using the SAS process. The effect of operating parameters on the particle size, crystal habit, and crystal form were evaluated. The choice of operation region was one of the key factors in the achievement of satisfactory recrystallization. Operation at a higher temperature that was slightly above the MCP of $\text{CO}_2 + \text{THF}$ was essential to obtain spherical crystals of sulfasalazine. The CO_2 flowrate and solution flowrate that modified the CO_2 mole fraction in the precipitator also had a considerable effect on recrystallization. Higher CO_2 flowrates and lower solution flowrates are recommended for the production of spherical particles. In this study, spherical particles with a mean size of $0.91 \mu\text{m}$ were successfully generated, with a satisfactory crystallization yield. These results proved that the SAS process is efficient in controlling the solid-state characteristics of APIs in the micronization and production of spherical crystals.

Supplementary Materials: The following are available online at <http://www.mdpi.com/2073-4352/8/7/295/s1>, Figure S1: DSC results of sulfasalazine crystals; Figure S2: PXRD results of sulfasalazine crystals.

Author Contributions: C.-S.S. designed the SAS experiments, prepared the original draft and revised the paper. W.-Y.W. performed the SAS experiments and analyzed the data.

Funding: The authors acknowledge financial support from the Ministry of Science and Technology Taiwan, MOST 106-2221-E-027-113-; MOST 107-3113-M-002-001-.

Conflicts of Interest: The authors declare no conflict of interest.

References

1. Kawakami, K. Modification of physicochemical characteristics of active pharmaceutical ingredients and application of supersaturatable dosage forms for improving bioavailability of poorly absorbed drugs. *Adv. Drug Deliver. Rev.* **2012**, *64*, 480–495. [[CrossRef](#)] [[PubMed](#)]
2. Khadka, P.; Ro, J.; Kim, H.; Kim, I.; Kim, J.T.; Kim, H.; Cho, J.M.; Yun, G.; Lee, J. Pharmaceutical particle technologies: An approach to improve drug solubility, dissolution and bioavailability. *Asian J. Pharm. Sci.* **2014**, *9*, 304–316. [[CrossRef](#)]
3. Jog, R.; Burgess, D.J. Pharmaceutical amorphous nanoparticles. *J. Pharm. Sci.* **2017**, *106*, 39–65. [[CrossRef](#)] [[PubMed](#)]
4. Modi, S.R.; Dantuluri, A.K.R.; Perumalla, S.R.; Sun, C.C.; Bansal, A.K. Effect of crystal habit on intrinsic dissolution behavior of celecoxib due to differential wettability. *Cryst. Growth Des.* **2014**, *14*, 5283–5292. [[CrossRef](#)]
5. Chattoraj, S.; Sun, C.C. Crystal and particle engineering strategies for improving powder compression and flow properties to enable continuous tablet manufacturing by direct compression. *J. Pharm. Sci.* **2018**, *107*, 968–974. [[CrossRef](#)] [[PubMed](#)]
6. Pudasaini, N.; Parker, C.R.; Hagen, S.U.; Bond, A.D.; Rantanen, J. Role of solvent selection on crystal habit of 5-aminosalicylic acid-combined experimental and computational approach. *J. Pharm. Sci.* **2018**, *107*, 1112–1121. [[CrossRef](#)] [[PubMed](#)]
7. Fahim, T.K.; Zaidul, I.S.M.; Abu Bakar, M.R.; Salim, U.M.; Awang, M.B.; Sahena, F.; Jalal, K.C.A.; Sharif, K.M.; Sohrab, M.H. Particle formation and micronization using non-conventional techniques-review. *Chem. Eng. Process.* **2014**, *86*, 47–52. [[CrossRef](#)]
8. Wu, J.J.; Shen, L.Y.; Yin, M.C.; Cheng, Y.S. Supercritical carbon dioxide anti-solvent micronization of lycopene extracted and chromatographic purified from *Momordica charantia* L. aril. *J. Taiwan Inst. Chem. Eng.* **2017**, *80*, 64–70. [[CrossRef](#)]
9. Wu, H.T.; Yang, C.P.; Huang, S.C. Dissolution enhancement of indomethacin-chitosan hydrochloride composite particles produced using supercritical assisted atomization. *J. Taiwan Inst. Chem. Eng.* **2016**, *67*, 98–105. [[CrossRef](#)]
10. Jung, J.; Perrut, M. Particle design using supercritical fluids: Literature and patent survey. *J. Supercrit. Fluids* **2001**, *20*, 179–219. [[CrossRef](#)]
11. Abuzara, S.M.; Hyuna, S.M.; Kim, J.H.; Park, H.J.; Kim, M.S.; Park, J.S.; Hwang, S.J. Enhancing the solubility and bioavailability of poorly water-soluble drugs using supercritical antisolvent (SAS) process. *Int. J. Pharm.* **2018**, *538*, 1–13. [[CrossRef](#)] [[PubMed](#)]
12. Yan, T.; Cheng, Y.; Wang, Z.; Huang, D.; Miao, H.; Zhang, Y. Preparation and characterization of baicalein powder micronized by the SEDS process. *J. Supercrit. Fluids* **2015**, *104*, 177–182. [[CrossRef](#)]
13. Jia, J.; Wang, W.; Gao, Y.; Zhao, Y. Controlled morphology and size of curcumin using ultrasound in supercritical CO₂ antisolvent. *Ultrason. Sonochem.* **2015**, *27*, 389–394. [[CrossRef](#)] [[PubMed](#)]
14. Reverchon, E.; Adami, R.; Campardelli, R.; Della Porta, G.; De Marco, I.; Scognamiglio, M. Supercritical fluids based techniques to process pharmaceutical products difficult to micronize: palmitoylethanolamide. *J. Supercrit. Fluids* **2015**, *102*, 24–31. [[CrossRef](#)]
15. Fernández-Ponce, M.T.; Masmoudi, Y.; Djerafi, R.; Casas, L.; Mantell, C.; Martínez de la Ossa, E.; Badens, E. Particle design applied to quercetin using supercritical anti-solvent techniques. *J. Supercrit. Fluids* **2015**, *105*, 119–127. [[CrossRef](#)]
16. Montes, A.; Pereyra, C.; Martínez de la Ossa, E.J. Screening design of experiment applied to the supercritical antisolvent precipitation of quercetin. *J. Supercrit. Fluids* **2015**, *104*, 10–18. [[CrossRef](#)]
17. Nerome, H.; Machmudah, S.; Wahyudiono; Fukuzato, R.; Higashiura, T.; Kanda, H.; Goto, M. Effect of solvent on nanoparticle production of β -carotene by a supercritical antisolvent process. *Chem. Eng. Technol.* **2016**, *39*, 1771–1777. [[CrossRef](#)]
18. Montes, A.; Wehner, L.; Pereyra, C.; Martínez de la Ossa, E.J. Generation of microparticles of ellagic acid by supercritical antisolvent process. *J. Supercrit. Fluids* **2016**, *116*, 101–110. [[CrossRef](#)]
19. Cheng, Y.; Xu, W.; Chen, Z.; Wang, Z.; Huang, D. Micronization of etoposide using solution-enhanced dispersion by supercritical CO₂. *J. Supercrit. Fluids* **2016**, *115*, 10–16. [[CrossRef](#)]

20. Kim, D.C.; Yeo, S.D. Modification of indomethacin crystals using supercritical and aqueous antisolvent crystallizations. *J. Supercrit. Fluids* **2016**, *108*, 96–103. [[CrossRef](#)]
21. Montes, A.; Wehner, L.; Pereyra, C.; Martínez de la Ossa, E.J. Mangiferin nanoparticles precipitation by supercritical antisolvent process. *J. Supercrit. Fluids* **2016**, *112*, 44–50. [[CrossRef](#)]
22. Montes, A.; Wehner, L.; Pereyra, C.; Martínez de la Ossa, E.J. Precipitation of submicron particles of rutin using supercritical antisolvent process. *J. Supercrit. Fluids* **2016**, *118*, 1–10. [[CrossRef](#)]
23. Yoon, T.J.; Son, W.S.; Park, H.J.; Seo, B.; Kim, T.; Lee, Y.W. Tetracycline nanoparticles precipitation using supercritical and liquid CO₂ as antisolvents. *J. Supercrit. Fluids* **2016**, *107*, 51–60. [[CrossRef](#)]
24. Jia, J.; Wang, J.; Zhang, K.; Zhou, D.; Ge, F.; Zhao, Y. Aescin nanoparticles prepared using SEDS: Composition stability and dissolution enhancement. *J. Supercrit. Fluids* **2017**, *130*, 267–272. [[CrossRef](#)]
25. Padrela, L.; Zeglinski, J.; Ryan, K.M. Insight into the role of additives in controlling polymorphic outcome: A CO₂-antisolvent crystallization process of carbamazepine. *Cryst. Growth Des.* **2017**, *17*, 4544–4553. [[CrossRef](#)]
26. Kurniawansyah, F.; Quachie, L.; Mammucari, R.; Foster, N.R. Improving the dissolution properties of curcumin using dense gas antisolvent technology. *Int. J. Pharm.* **2017**, *521*, 239–248. [[CrossRef](#)] [[PubMed](#)]
27. Liu, G.; Lin, Q.; Huang, Y.; Guan, G.; Jiang, Y. Tailoring the particle microstructures of gefitinib by supercritical CO₂ antisolvent process. *J. CO₂ Utiliz.* **2017**, *20*, 43–51. [[CrossRef](#)]
28. Kudryashova, E.V.; Deygen, I.M.; Sukhoverkov, K.V.; Filatova, L.Y.; Klyachko, N.L.; Vorobei, A.M.; Pokrovskiy, O.I.; Ustinovich, K.B.; Parenago, O.O.; Antonov, E.N.; et al. Micronization of levofloxacin by supercritical antisolvent precipitation. *Russ. J. Phys. Chem. B* **2016**, *10*, 1201–1210. [[CrossRef](#)]
29. Miao, H.; Chen, Z.; Xu, W.; Wang, W.; Song, Y.; Wang, Z. Preparation and characterization of naringenin microparticles via a supercritical anti-solvent process. *J. Supercrit. Fluids* **2018**, *131*, 19–25. [[CrossRef](#)]
30. Chen, H.H.; Su, C.S. Recrystallizing primidone through supercritical antisolvent precipitation. *Org. Process Res. Dev.* **2016**, *20*, 878–887. [[CrossRef](#)]
31. Ciou, J.M.; Wang, B.C.; Su, C.S.; Liu, J.J.; Sheu, M.T. Measurement of solid solubility of warfarin in supercritical carbon dioxide and recrystallization study using supercritical antisolvent process. *Adv. Powder Technol.* **2018**, *29*, 479–487. [[CrossRef](#)]
32. Wu, W.Y.; Su, C.S. Modification of solid-state property of sulfasalazine by using the supercritical antisolvent process. *J. Cryst. Growth* **2017**, *460*, 59–66. [[CrossRef](#)]
33. Campardelli, R.; Reverchon, E.; De Marco, I. Dependence of SAS particle morphologies on the ternary phase equilibria. *J. Supercrit. Fluids* **2017**, *130*, 273–281. [[CrossRef](#)]



© 2018 by the authors. Licensee MDPI, Basel, Switzerland. This article is an open access article distributed under the terms and conditions of the Creative Commons Attribution (CC BY) license (<http://creativecommons.org/licenses/by/4.0/>).